

Single atom Ru-supported reduced graphene oxide integrated self-assembled monolayer as a nm-scale Cu diffusion barrier

Received: 23 December 2024

Sibo Zhao¹, Dewei Zhang², Guoxiang Cui¹, Xiangyu Ren¹, Shenghong Ju^{2,3}✉, Tao Hang¹, Ming Li¹ & Yunwen Wu^{1,4}✉

Accepted: 5 December 2025

Published online: 20 December 2025

 Check for updates

In advanced integrated circuits, signal transmission delay arising from interconnect resistance is a main problem hindering the development of electronic devices, while the conventional several-nanometer-thick TaN/Ta barrier with high resistivity causes a surge in interconnect resistance due to the size effect. To address this issue, it is crucial to develop Cu barrier materials. Here, we design an integrated ultra-thin Cu diffusion barrier (~1.4 nm) consisting of single-atom Ru-supported reduced graphene oxide (Ru SA-rGO) and self-assembled monolayer (SAM) derived from (3-aminopropyl)triethoxysilane, which combines the dual functions of liner and barrier. The supporting of Ru requires N-doping as a bridge. Remarkably, the mean time-to-failure of devices with Ru SA-rGO/SAM is approximately 24 times longer than barrier-free devices. Ru atoms can both physically block Cu diffusion by filling rGO vacancies and chemically capture Cu through enhanced adsorption. Our work provides insight into diffusion barrier development in advanced Cu interconnects.

Under the post Moore era, as chip integration continues to increase in the Integrated Circuit (IC) industry, the feature size of interconnects has been shrinking continuously¹. The pivotal factor limiting the performance of electronic devices is no longer the processing speed of transistors, but rather the issues of signal transmission delay and reliability arising from interconnects^{2,3}. The barrier/liner (TaN/Ta) bilayer, composed of TaN with strong ability to block Cu diffusion and Ta with effective adhesion to Cu, has been widely used in interconnects for a considerable period^{4,5}. Nevertheless, as the interconnection line width decreases, the proportion of TaN/Ta occupying the total cross-sectional area of the interconnect continues to increase. Consequently, the high resistivity of TaN/Ta becomes increasingly detrimental to the line conductivity, leading to severe signal transmission delay^{6–8}. Therefore, research needs to be conducted on new interconnect barrier materials that can fulfill three key criteria: ultra-thin, high conductivity, and excellent diffusion barrier property (Fig. 1a)^{9,10}.

In recent years, researchers have focused on and conducted extensive studies in three main directions for diffusion barriers: self-forming alloys^{11,12}, self-assembled monolayers (SAM)^{13,14}, and two-dimensional (2D) materials^{15–19}. It has been demonstrated that both the alkyl chain and the terminal group of the SAM have a crucial influence on its diffusion barrier properties^{20–25}. Caro et al. found that a NH₂-terminated SAM derived from (3-aminopropyl)trimethoxysilane (APTMS) exhibited the best compatibility for Cu interconnects among the analyzed SAMs with a variety of terminal groups and chain lengths²⁰. Further studies have shown that by chemically modifying the terminal groups of APTMS or coupling it with other molecules, the diffusion barrier properties, adhesion to Cu, and conductivity of the resulting SAMs can be respectively enhanced^{23–25}. Generally, SAMs on SiO₂ can achieve an ultra-thin film of less than 1 nm while maintaining satisfactory uniformity and continuity. However, SAMs start to desorb from SiO₂ (250 °C) or even decompose (350 °C) below the operating temperature for back-end-of-line (BEOL) process^{26,27}. This low thermal

¹School of Material Science and Engineering, Shanghai Jiao Tong University, Shanghai, China. ²China-UK Low Carbon College, Shanghai Jiao Tong University, Shanghai, China. ³Key Laboratory for Thermal Science and Power Engineering of Ministry of Education, Department of Engineering Mechanics, Tsinghua University, Beijing, China. ⁴National Key Laboratory of Advanced Micro and Nano Manufacture Technology, Shanghai Jiao Tong University, Shanghai, China.

✉ e-mail: jush@tsinghua.edu.cn; tlwuyunwen@sjtu.edu.cn

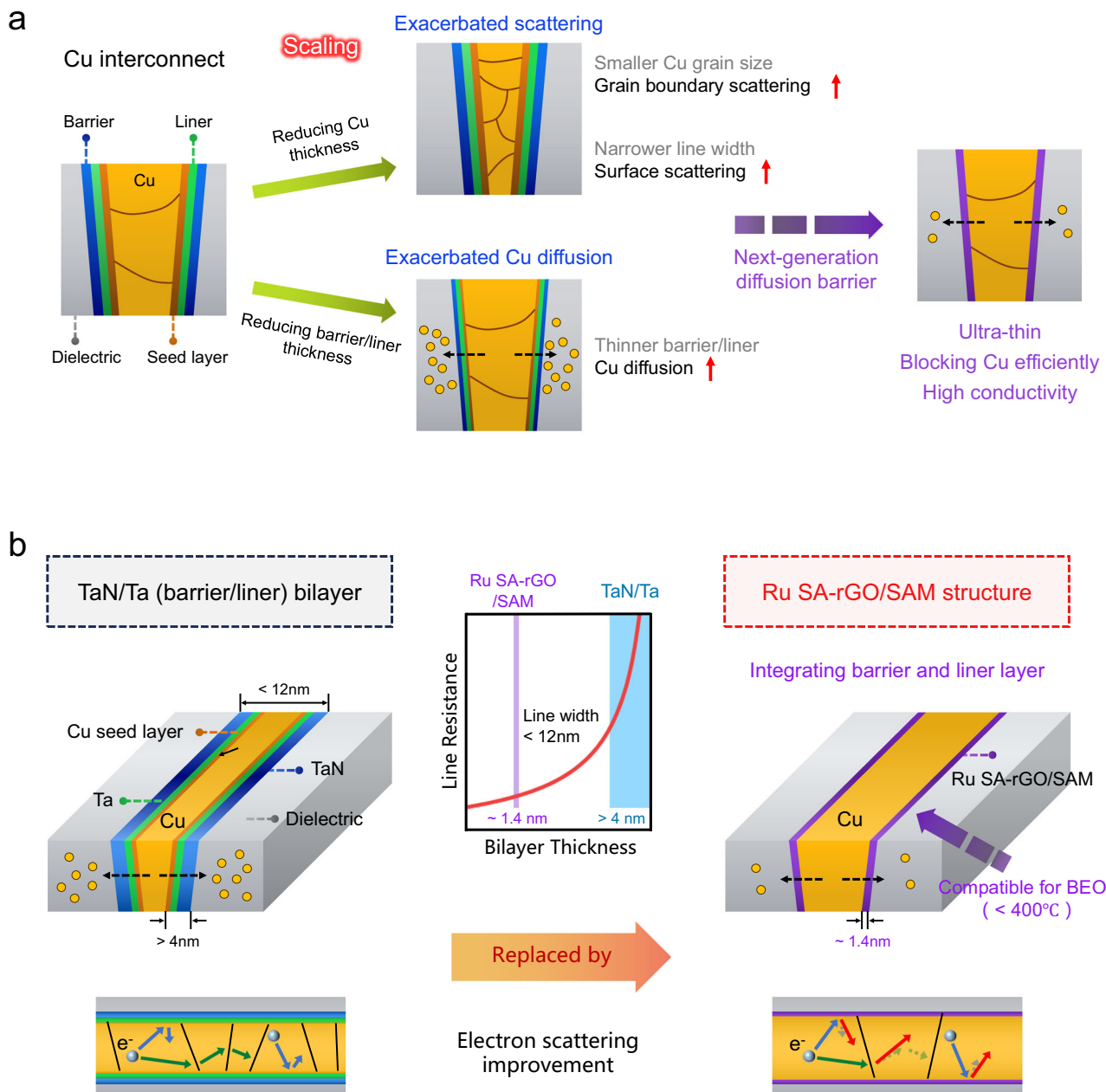


Fig. 1 | The challenges posed by the scaling of Cu interconnect and the requirements for the materials available for the next-generation diffusion barrier. **a** The schematic diagram representative of the damascene structure of Cu interconnect. **b** Comparison between the diffusion barrier fabricated in this work

(Ru SA-rGO/SAM structure) and the conventional TaN/Ta bilayer. The diffusion barrier presented in this work simultaneously meets the requirements of ultra-thin, excellent diffusion barrier properties, high conductivity, and compatibility with BEOL process.

stability of SAMs may significantly damage the interconnection performance.

2D materials have the potential to be the next-generation interconnect barrier due to their distinctive structural characteristics¹⁰, such as graphene^{15,28,29}, hexagonal boron nitride (h-BN)^{16,30}, and transition metal dichalcogenides (TMDs)^{19–21}. Among these 2D materials, graphene stands out because of its ultrahigh carrier mobility³¹. The graphene-copper integrated structure facilitates charge transfer at the interface, effectively enhancing interconnect conductivity^{32–34}. Furthermore, graphene has excellent properties to block vertical Cu diffusion^{35,36}. Research by Li et al. demonstrated that single-layer graphene with a thickness of 0.35 nm exhibits diffusion barrier property comparable to 4 nm TaN²⁸. Additionally, graphene exhibits high thermal stability against Cu diffusion. Even under thermal stress

conditions of 700 °C for 30 min, thermal diffusion does not occur in 1 nm thick tri-layer graphene¹⁵. For a long time, the high growth temperature of graphene during chemical vapor deposition (CVD), along with macroscopical transfer defects, such as folds, cracks and tears, have presented challenges in applying graphene as a diffusion barrier in BEOL processes^{10,37–41}. Recent researches have shown that graphene can now be directly deposited on SiO₂ at a low temperature⁴², and the stacking of wafer-scale ultra-flat graphene with scarce transfer defects has been achieved through flat-to-flat transfer process⁴³. However, graphene exhibits poor adhesion to Cu due to its intrinsic weak van der Waals interaction between layers^{10,44}. Moreover, the rapid migration of Cu atoms or ions between graphene layers limits the improvement of its diffusion barrier properties, especially when increasing the number of graphene stacking

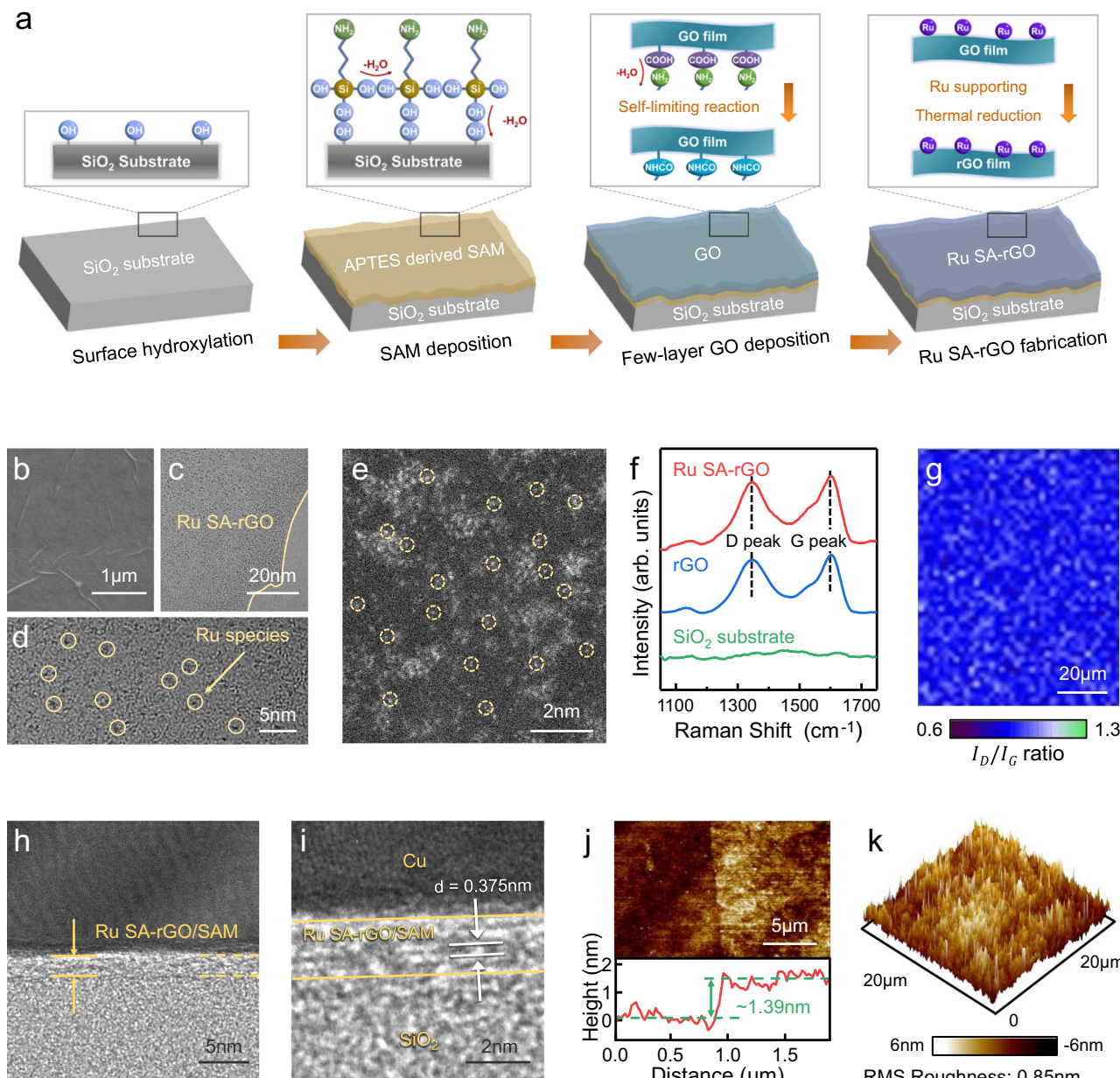


Fig. 2 | Synthesis and Characterization of Single Atom Ru-supported (Ru SA)-rGO/SAM. **a** Synthesis strategy of Ru SA-rGO/SAM structure. **b** SEM, **c** TEM, **d** HRTEM and **e** HAADF-STEM images of Ru SA-rGO. **f** Raman spectra including SiO₂ substrate, pristine rGO and Ru SA-rGO. **g** Raman mapping of the I_D/I_G ratio of Ru

SA-rGO. **h** TEM and **i** HRTEM images of the cross section of Ru SA-rGO/SAM. **j** AFM image of Ru SA-rGO/SAM, measuring its thickness to be ~1.39 nm. **k** AFM 3D image of Ru SA-rGO/SAM, measuring its RMS roughness to be 0.85 nm. Source data are provided as a Source Data file.

layers²⁸. These factors restrict the potential application of graphene as a diffusion barrier.

In this work, we designed an integrated diffusion barrier structure consisting of a single-atom Ru-supported reduced graphene oxide (Ru SA-rGO) and a SAM derived from (3-aminopropyl)triethoxysilane (APTES). Compared to graphene, graphene oxide (GO) introduces numerous oxygen-containing functional groups at its surface and edges⁴⁵, which enable a stable combination between GO and SAM through reaction with the terminal groups in SAM⁴⁶. Through the support of Ru species on GO/SAM, combined with a subsequent thermal reduction process, the Ru SA-rGO/SAM structure was successfully synthesized in a BEOL-compatible temperature. The results indicate that the Ru SA-rGO/SAM structure, integrates the dual functions of liner and diffusion barrier with its ultra-thin thickness, achieving a combination of good adhesion to Cu and excellent

thermal/electrical diffusion barrier properties. Moreover, the critical role of Ru in the superior properties of Ru SA-rGO/SAM has been verified through calculations. It can be expected that the ultra-thin Ru SA-rGO/SAM diffusion barrier can significantly benefit the interconnect performance (Fig. 1b).

Results

Synthesis and characterization of Ru SA-rGO/SAM

Figure 2a illustrates the synthesis process of Ru SA-rGO/SAM structure on SiO₂ substrate. Firstly, surface-hydroxylated SiO₂ was achieved through Piranha solution etching. Molecule adsorption was then carried out via hydrogen bonding between hydrolyzed APTES and surface-hydroxylated SiO₂, followed by a transformation from the initial hydrogen bonding to strong covalent bonding through dehydration reaction⁴⁷. After the deposition of an atomic-scale thickness

SAM, a uniform few-layer GO was fabricated on it through an electro-assisted self-limiting deposition process⁴⁸. The reaction between the carboxyl groups (-COOH) in GO and the amino terminal groups (-NH₂) in APTES contributes to the self-limiting deposition. Scanning electron microscopy (SEM) image of few-layer GO deposited on SAM was observed in supplementary Fig. 1, where the wrinkled feature represents the stacking morphology of GO. The support of Ru species onto GO requires a N-doping process as a bridge. As the nitrogen source, aniline firstly stacked on GO through π - π interactions using edge-to-face model⁴⁹. Ru species were then coordinated with the -NH₂ of aniline. Through a final thermal reduction process, the N species were inserted into the GO skeleton while the Ru species were immobilized by complexation reaction. The SEM image of the fabricated Ru-supported rGO is shown in Fig. 2b.

The morphology of Ru-supported rGO was characterized by transmission electron microscopy (TEM) and high-resolution TEM (HRTEM). As shown in Fig. 2c, Ru species, appearing as black dots in the TEM image, were well-dispersed on the surface of GO. In the HRTEM image (Fig. 2d), the supported Ru species (highlighted by yellow circles) exhibit lattice fringes that are significantly distinct from the surrounding GO matrix, demonstrating the successful support of Ru species on GO. To further explore the support configuration of Ru species, high-angle annular dark-field scanning TEM (HAADF-STEM) was employed. Due to the contrast in HAADF-STEM being proportional to the square of the atomic number (Z²), the Ru species possess remarkably higher contrast compared to the C and N species in the matrix. The distribution of numerous discrete bright spots seen in Fig. 2e indicates that the Ru species were supported as individual single atoms.

Figure 2f shows the comparison of Raman spectra between SiO₂ substrate and the Ru SA-rGO fabricated on this substrate. The Ru SA-rGO exhibits two prominent Raman peaks at 1346 and 1604 cm⁻¹, which are well-matched with the D and G bands of graphene, respectively. In contrast, the SiO₂ substrate lacks these peaks. The D-to-G band intensity ratio (I_D/I_G) is widely recognized as an important parameter for evaluating the defect density and degree of graphitization in carbonaceous materials⁵⁰. As shown in Fig. 2g, the I_D/I_G of Ru SA-rGO is concentrated around 0.85. This demonstrates the uniformity of the fabricated Ru SA-rGO, yet it does not exhibit a high degree of graphitization, which verifies the mostly amorphous tendency observed in the TEM images.

Figure 2h, i reveal the cross-sectional morphology of Ru SA-rGO/SAM structure. In the TEM image (Fig. 2h), the Ru SA-rGO/SAM layer on SiO₂ substrate exhibits a tightly adhered interface with no noticeable protrusions or unevenness. As shown in Fig. 2i, compared to the regular lattice fringes of graphene, the lattice fringes exhibited by Ru SA-rGO mostly tend to be amorphous. This amorphous characteristic of Ru SA-rGO ensures its ability to block the lateral migration of Cu as a diffusion barrier. The interplanar spacing of Ru SA-rGO analyzed by fast Fourier transform (FFT) is about 0.375 nm, which is slightly higher than the interplanar spacing of rGO (~0.35 nm)⁵¹. This may be due to the support of Ru atoms on rGO, whose atomic volume much larger than that of carbon.

The thickness and roughness of Ru SA-rGO/SAM were directly measured by atomic force microscopy (AFM). As shown in Fig. 2j, the thickness of Ru SA-rGO/SAM is approximately 1.39 nm, which includes a 0.37 nm SAM confirmed by ellipsometer. Meanwhile, the root mean square (RMS) roughness of Ru SA-rGO/SAM was determined to be 0.85 nm over a 20 \times 20 μm measurement area (Fig. 2k). To verify the uniformity of the diffusion barrier, we fabricated a 20 \times 20 mm Ru SA-rGO/SAM/SiO₂ sample and performed AFM analysis across five distinct regions (20 \times 20 μm measurement area), as shown in supplementary Fig. 3. The results reveal consistent roughness values averaging 0.87 nm with only 0.091 nm variation between maximum and minimum measurements, demonstrating

high macroscopic uniformity of Ru SA-rGO/SAM throughout the sample.

To clarify the configuration of N and Ru species in Ru SA-rGO/SAM, X-ray photoelectron spectroscopy (XPS) was employed on SAM, N-rGO/SAM (only conducted N-doping process), and Ru SA-rGO/SAM (conducted both N-doping and Ru-supporting process). The N-doping process typically introduces four distinct N-containing species: pyridinic N, pyrrolic N, graphitic N and oxidized N, whose configurations are shown in Fig. 3a⁵². Graphitic N mainly fills the point defects in rGO, while pyridinic N and pyrrolic N can repair larger vacancies or establish connections at the edges of rGO.

The C 1s spectra of the three samples are shown in Fig. 3b. Notably, a small peak can be clearly observed at a position deviating from the main C 1s spectra of Ru SA-rGO/SAM, which can be attributed to the Ru 3d spectra. The successful supporting of Ru species can be further validated by the appearance of the Ru 3p peak in the XPS survey spectra (supplementary Fig. 6). The Ru 3d_{5/2} peak of Ru SA-rGO/SAM at 281.8 eV is situated between Ru⁰ (279.75 eV) and Ru³⁺ (282.4 eV)⁵³. It is suggested that the valence state of the supported Ru is between 0 and +3. Additionally, the much lower intensity of the Ru 3d_{5/2} peak compared to the C 1s peaks indicates a low content of Ru supported on rGO.

As shown in Fig. 3c, the N 1s spectra of SAM reveals three distinct peaks, corresponding to amino at 399.7 eV, hydrogen-bonded nitrogen (H-bonded N) at 401.5 eV, and oxidized N at 403.3 eV, respectively²⁵. The strong peak of H-bonded N might originate from the hydrogen bonding between amino groups in APTES with each other or with hydroxyl groups on SiO₂ substrate¹³. In contrast, the N 1s spectra of N-rGO/SAM and Ru SA-rGO/SAM exhibit three new components, which are assigned to indexed to pyridinic N (398.4 eV), pyrrolic N (400.3 eV), graphitic N (401.5 eV)⁵².

To further investigate the interaction between Ru and N species in rGO, we conducted a comprehensive analysis of XPS peak positions. Compared to N-rGO/SAM, the binding energy of pyridinic N and pyrrolic N in Ru SA-rGO/SAM shifts 0.2 eV higher, while the binding energy of amino and graphitic N remains unchanged (supplementary Table 1). This indicates that pyridinic N and pyrrolic N play a role in coordinating with Ru atoms, leading to a change in their electronic state, while amino and graphitic N scarcely participate in the coordination¹³. Meanwhile, the binding energies of the C sp² and C sp³ peaks in the C 1s spectra also show no change (supplementary Table 2). This reveals that very few Ru atoms are adsorbed on the lattice of rGO. The adsorption energy (ΔE_{ads}) results from density functional theory (DFT) calculations further support this conclusion, as shown in Fig. 3d. A more negative ΔE_{ads} indicates a higher tendency for Ru atoms to be adsorbed on the specific N-doped structures. Compared to graphitic N (~-3.42 eV), Ru atoms exhibit much lower ΔE_{ads} for pyridinic N (~-9.77 eV) and pyrrolic N (~-12.18 eV), indicating the preferential adsorption of Ru atoms on pyridinic N and pyrrolic N. Furthermore, the optimized structure shows that Ru atoms tend to be located at the vacancies within the plane of rGO when adsorbed on pyridinic N and pyrrolic N. This suggests that the supported Ru atoms can effectively fill the defects in rGO. Ru atoms were replaced by Cu atoms to calculate ΔE_{ads} under the same structures. The results show that the ΔE_{ads} of Cu atoms is significantly more positive than that of Ru atoms in each N-doped structure, which proves that the supported Ru will not desorb due to the introduction of Cu (supplementary Fig. 7 and 8).

Adhesion to Cu

The tape test method was employed to verify the adhesion of Cu on Ru SA-rGO/SAM. After successfully preparing Ru SA-rGO/SAM on a SiO₂ substrate, a ~25 nm Cu film was deposited by vacuum evaporation. The adhesion test was conducted using 3 M tape by contacting and then removing it. After the removal of the 3 M tape, the Cu film remained only in the regions with Ru SA-rGO/SAM, as shown in Fig. 4a and

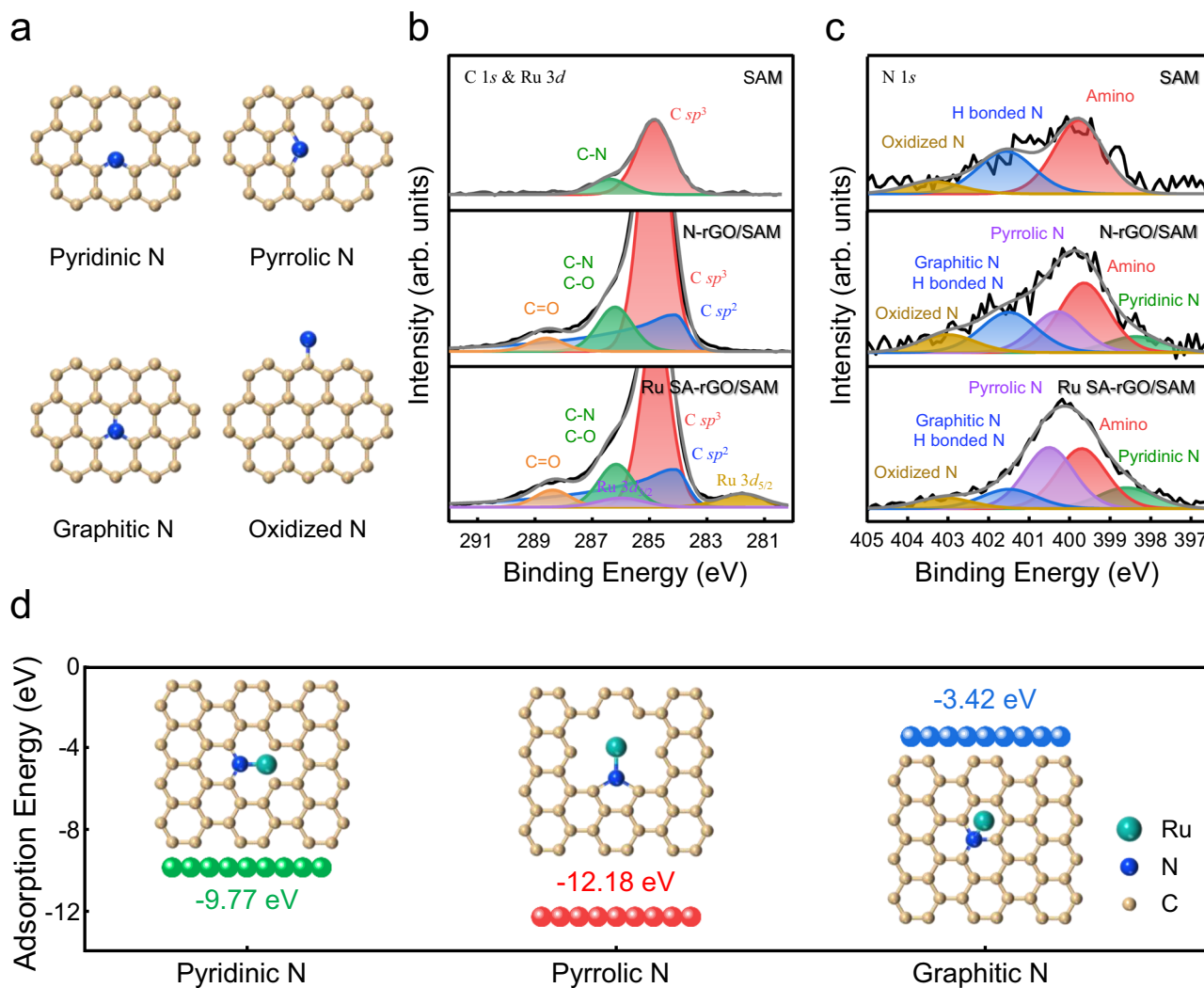


Fig. 3 | Identification of the configuration of N and Ru species in single atom Ru-supported (Ru SA)-rGO. a Schematic diagram showing the configuration of nitrogen species doped into rGO lattice. **b** XPS C 1s spectra of SAM, N-rGO/SAM, and Ru SA-rGO/SAM (from top to bottom). **c** XPS N 1s spectra of SAM, N-rGO/SAM, and Ru SA-rGO/SAM (from top to bottom). **d** The optimized structures and the

adsorption energies for Ru-pyridinic N, Ru-pyrrolic N and Ru-graphitic N configurations. The structures were optimized by DFT calculations within the generalized gradient approximation and GGA-PBE approximation, as implemented in the VASP package. Source data are provided as a Source Data file.

supplementary Fig. 9. AFM analysis indicates that after the tape adhesion test, the thickness difference at the interface with and without Ru SA-rGO/SAM is approximately 25 nm (Fig. 4b), which corresponds to the deposited thickness of the Cu film. In addition, the Cu film deposited on Ru SA-rGO/SAM shows no significant thickness fluctuations after the tape adhesion test, as shown in Fig. 4c. These results suggest that the Cu film deposited on the Ru SA-rGO/SAM layer was almost unaffected by the tape.

After annealing the samples at 500 °C for 30 min, it was observed that the Cu film deposited on the SiO₂ substrate cracked and aggregated into numerous spherical particles, as shown in Fig. 4d (The SEM images of the samples before annealing are shown in supplementary Fig. 10). In contrast, the sample with Ru SA-rGO/SAM maintained the integrity of the Cu film due to its strong adhesion (Fig. 4e). We deposited thicker Cu films (~1 μm) on samples with and without Ru SA-rGO/SAM, and further examined the interface adhesion using cross-sectional SEM. The interface between Ru SA-rGO/SAM and the Cu film is tightly bonded (supplementary Fig. 11b), whereas there is a noticeable separation between the substrate without Ru SA-rGO/SAM and the Cu film (supplementary Figs. 11a and 12). All the results indicate that the Ru SA-rGO/SAM layer exhibits excellent adhesion to Cu.

To quantitatively evaluate the interfacial adhesion strength, four-point bending tests were performed for both Cu/SiO₂ and Cu/Ru SA-rGO/SAM/SiO₂ structures. The load-displacement curves of both structures are shown in supplementary Fig. 13. The results indicate that the interfacial delamination occurred at 4.07 N for Cu/SiO₂ and at 6.08 N for Cu/Ru SA-rGO/SAM/SiO₂. We further quantitatively evaluate the interfacial adhesion energy of the two structures based on the calculation equation for interfacial adhesion energy (G_c)⁵⁴

$$G_c = \frac{21(1 - \nu_s^2)P_c^2L^2}{16E_sB^2h^3} \quad (1)$$

where P_c is the critical load for interface delamination, L is the distance between the loading and supporting points (7 mm), B is specimen width (5 mm), h is substrate thickness (525 μm), E_s is Young's modulus (130 GPa), and ν_s is Poisson's ratio (0.28). The calculated G_c values of both configurations are displayed in supplementary Table 3. The result reveals a significant increase from 2.1 to 4.7 J m⁻² after the introduction of Ru SA-rGO/SAM, which effectively validates enhanced interfacial adhesion.

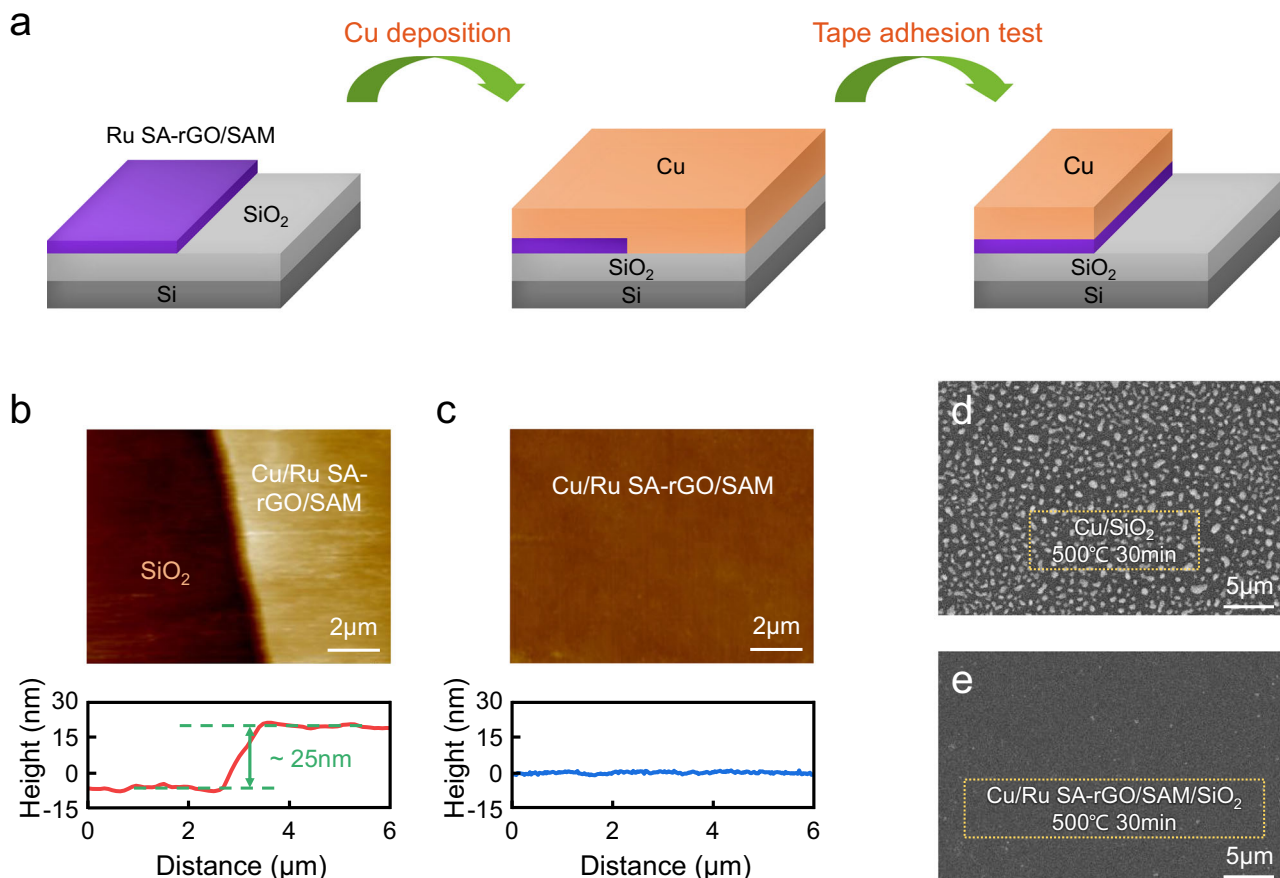


Fig. 4 | Adhesion of single atom Ru-supported (Ru SA)-rGO/SAM to Cu.

a Schematic diagram of tape adhesion test. b AFM image of the interface between Cu/Ru SA-rGO/SAM and SiO₂. c AFM image of the Cu/Ru SA-rGO/SAM structure.

SEM images of d Cu/SiO₂ and e Cu/Ru SA-rGO/SAM/SiO₂ after annealing at 500 °C for 30 min. Source data are provided as a Source Data file.

Thermal stability and ability to block Cu thermal diffusion

To evaluate the thermal stability of Ru SA-rGO/SAM structure and its ability to block Cu thermal diffusion, a 50 nm-thick Cu film was deposited on a Ru SA-rGO/SAM/SiO₂/Si sample. For comparison, in addition to directly depositing 50 nm Cu film on SiO₂/Si without diffusion barrier, we also prepared samples with a diffusion barrier of a single SAM or pristine rGO/SAM, respectively. All samples were annealed at temperatures ranging from 400 °C to 600 °C for 30 min in an argon atmosphere. The thermal diffusion failure mechanism of Cu interconnects is shown in Fig. 5a. For samples without diffusion barrier, Cu atoms may easily infiltrate into the dielectric as the temperature increases. Subsequently, Cu reacts with Si to form intermetallic compounds (Cu_xSi_y) at the interface, leading to ultimate failure of devices. In contrast, the addition of a diffusion barrier can significantly suppress Cu diffusion, thereby delaying failure arising from the formation of Cu_xSi_y.¹⁵

After annealing the Cu/Ru SA-rGO/SAM/SiO₂ structure at 600 °C for 30 min, cross-sectional observation (Fig. 5b) indicates that the Ru SA-rGO/SAM layer remained intact, with no significant formation of Cu_xSi_y intermetallic compounds at the interface. STEM-energy dispersive X-ray spectroscopy (STEM-EDS) further confirms that, due to the presence of the Ru SA-rGO/SAM diffusion barrier, there was negligible diffusion of Cu atoms into the SiO₂ during annealing (Fig. 5c–f). These results demonstrate that the Ru SA-rGO/SAM diffusion barrier exhibits excellent thermal stability and remarkable resistance to Cu thermal diffusion.

According to the failure mechanism, X-ray diffraction (XRD) analysis was conducted for phase identification. Figure 5g illustrates

the variation of XRD patterns for samples with different diffusion barriers in various annealing conditions. Except for the diffraction peaks of substrate, it can be easily observed that two types of intermetallic compounds, Cu₃Si and Cu₁₅Si₄, were generated during the annealing process. The diffraction peaks at 27.9°, 35.2°, 42.4°, and 49.5°, are respectively identified as (020), (021), (030), and (301) of Cu₃Si, while diffraction peaks at 29.4°, 46.1°, 48.1°, and 53.7°, are respectively indexed as (310), (422), (510), and (440) of Cu₁₅Si₄.^{15,55,56} After annealing at 400 °C for 30 min, Cu_xSi_y peaks start to appear in samples without diffusion barrier and only with SAM diffusion barrier, which proves the low thermal stability of SAM. As the temperature rises to 500 °C, the rGO/SAM diffusion barrier quickly fails, accompanied by the extensive formation of Cu_xSi_y. Only the samples with Ru SA-rGO/SAM diffusion barrier still retain the ability to block Cu diffusion at 600 °C (Ru SA-rGO/SAM starts to fail at 700 °C, as shown in supplementary Fig. 14). This indicates that the Ru-supporting process is a key factor contributing to the excellent ability of Ru SA-rGO/SAM diffusion barrier to block Cu diffusion.

Electrical diffusion barrier properties

The electrical properties of the Ru SA-rGO/SAM structure were evaluated by electrical tests, including current-voltage (I-V) measurements and time-dependent dielectric breakdown (TDDB) measurements. To enable direct comparison of electrical diffusion barrier properties between Ru SA-rGO/SAM and TaN/Ta structure, we deposited a TaN/Ta bilayer with a total thickness of 6.27 nm on SiO₂ substrate, as illustrated in supplementary Fig. 15. For both electrical tests, a simplified metal-oxide-semiconductor (MOS) capacitor structure was prepared,

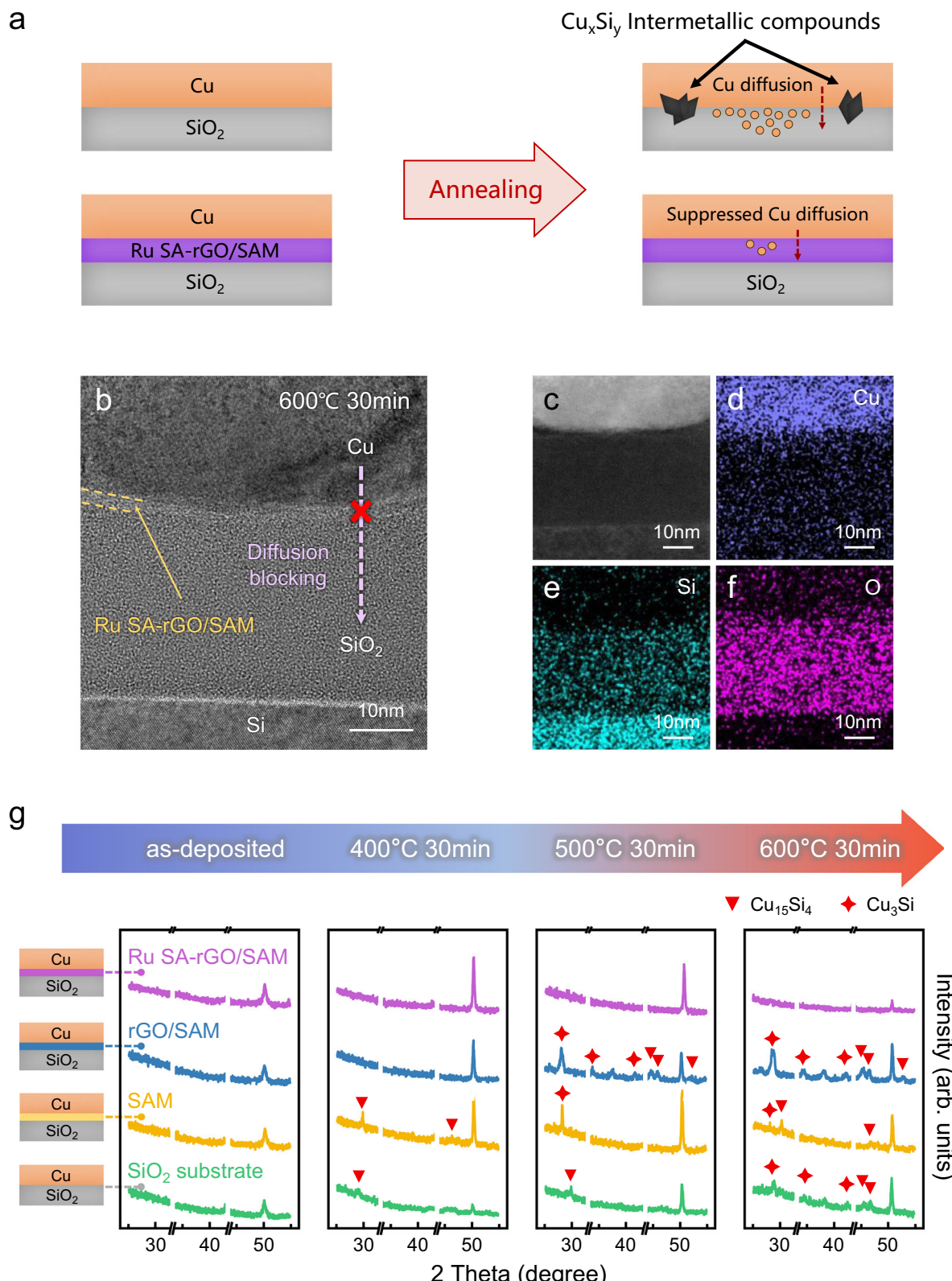
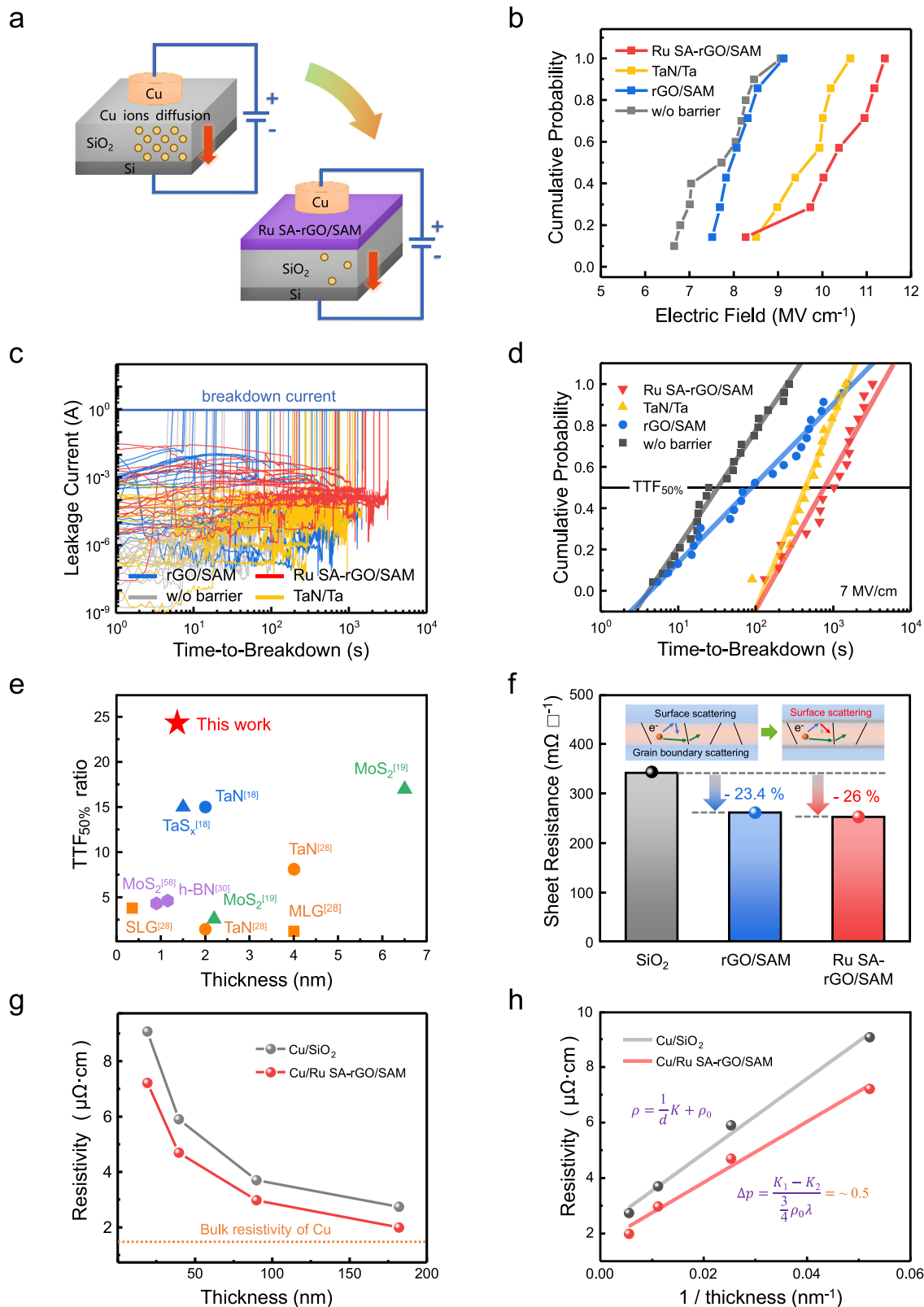


Fig. 5 | Ability of single atom Ru-supported (Ru SA)-rGO/SAM to block Cu thermal diffusion. **a** Schematic diagram of thermal diffusion failure mechanism of Cu interconnects. **b** HRTEM image, **c** HAADF-STEM image, and STEM-EDS mapping of **d** Cu, **e** Si and **f** O of the cross section of Cu/Ru SA-rGO/SAM/SiO₂/Si structure

after annealing at 600 °C for 30 min. **g** XRD patterns of samples including Cu/SiO₂, Cu/SAM/SiO₂, Cu/rGO/SAM/SiO₂, and Cu/Ru SA-rGO/SAM/SiO₂ under different annealing conditions (As-deposited, 400 °C 30 min, 500 °C 30 min, and 600 °C 30 min). Source data are provided as a Source Data file.



as depicted in Fig. 6a. A vertical electric field was applied across the capacitor structure, driving the migration of Cu ions into the dielectric. As the electric field intensity increases or the time prolongs, a large number of Cu ions form conducting paths in the dielectric, causing breakdown failure of the capacitor structure⁵⁷. The presence of a diffusion barrier can extend the lifetime of devices by preventing the migration of Cu ions.

I-V measurement indicates the variation of leakage current with the electric field intensity. It is considered as breakdown failure of devices when the leakage current abruptly jumps and exceeds a certain value. The voltage is recorded when the current jump occurs to evaluate the critical electric field (E_c) of each device. We conducted I-V measurements on multiple devices with different diffusion barriers, and the variation of leakage current with the applied electric field is

Fig. 6 | Electrical diffusion barrier properties and conductivity of single atom Ru-supported (Ru SA)-rGO/SAM. **a** Schematic diagram of failure mechanism of Cu interconnects under electric field. **b** I-V measurement including devices without diffusion barrier and devices with rGO/SAM, TaN/Ta and Ru SA-rGO/SAM diffusion barrier. **c** Time-to-breakdown of devices tested by TDDB measurement. **d** Statistical distribution of time-to-breakdown of devices. **e** Comparison of TTF_{50%} ratio and thickness of the Ru SA-rGO/SAM developed in this work with those reported in recent research (details shown in supplementary Table 5). **f** Sheet resistance of

devices with different diffusion barriers. **g** Resistivity of Cu films varying thicknesses (19.2 nm - 182 nm) on SiO₂ substrate and Ru SA-rGO/SAM. **h** Linear fitting of the resistivity (ρ) versus inverse thickness (1/d) relationship for Cu films on SiO₂ substrate and on Ru SA-rGO/SAM. The coefficients of determination (R^2) are 0.99 for Cu/SiO₂ and 0.98 for Cu/Ru SA-rGO/SAM. By comparing the slope difference between two curves, the surface scattering parameter of the two structures are calculated to differ by $\Delta p = -0.5$. Source data are provided as a Source Data file.

shown in supplementary Fig. S16. The E_c values of devices were further plotted in Fig. 6b, and the cumulative probability represents the E_c values from low to high. Compared to devices without diffusion barrier (7.7 MV cm⁻¹), devices with rGO/SAM (8.2 MV cm⁻¹), TaN/Ta (9.7 MV cm⁻¹), and Ru SA-rGO/SAM (10.3 MV cm⁻¹) diffusion barriers correspond to an increase in the mean E_c value by 5.6%, 26.0%, and 33.1%, respectively.

TDDB measurement is used to evaluate the lifetime of devices at a constant electric field. The abrupt jump in leakage current indicates the breakdown failure of devices, similar to I-V measurement. Figure. 6c illustrates the variation of leakage current with the stress time under an electric field of 7 MV cm⁻¹. It can be observed that although devices with TaN/Ta bilayer exhibit significantly longer time-to-breakdown overall compared to barrier-free devices, those featuring the Ru SA-rGO/SAM diffusion barrier show even longer time-to-breakdown. The statistical distribution of time-to-breakdown of devices is shown in Fig. 6d. For each type of devices, linear fitting was performed between the time-to-breakdown and cumulative probability. Each fitting presents great accuracy with a coefficient of determination (R^2) above 0.95. Based on this, mean time-to-failure (TTF_{50%}) was obtained by determining the time-to-breakdown corresponding to the cumulative probability of 0.5 for the fitting line, which serves as an overall evaluation of the lifetime of devices. Compared to the devices without diffusion barrier (~33 s), TTF_{50%} is approximately 3, 14, and 24 times longer for devices with rGO/SAM (~91 s), TaN/Ta (~441 s), and Ru SA-rGO/SAM (~773 s) diffusion barrier, respectively. The results of TDDB measurement can be matched with those of IV measurement, collectively demonstrating that the Ru SA-rGO/SAM diffusion barrier exhibits superior electrical diffusion barrier performance compared to TaN/Ta bilayer. Additionally, similar to the thermal test results, all electrical test results reveal that the Ru-supporting process is the critical factor for achieving outstanding electrical properties.

Figure. 6e compares the TTF_{50%} ratio and thickness in this work with those reported in recent research. Given the inconsistent electric field and temperature conditions used for TDDB measurement in different reports, the classic E-model is employed to normalize the data²⁸

$$TTF50\% \propto \exp\left(\frac{\Delta H_a}{k_b T} - \gamma E_s\right) \quad (2)$$

where ΔH_a represents the activation energy of dielectric breakdown, k_b is the Boltzmann constant, γ is the electric field factor, E_s represents the electric field applied to the dielectric. The TTF_{50%} value with $E_s = 7$ MV cm⁻¹, $T = 298.15$ K is determined as the normalized TTF_{50%} value. To compare the improvement in lifetime of devices by adding diffusion barrier, the ratio of the normalized TTF_{50%} value of devices with each type of diffusion barrier to that of devices without diffusion barrier can be considered as a relative parameter to assess the diffusion barrier properties, which can be expressed as:

$$TTF50\% \text{ratio} = \frac{TTF50\% \text{with barrier}(7\text{MVcm}^{-1}, 25^\circ\text{C})}{TTF50\% \text{without barrier}(7\text{MVcm}^{-1}, 25^\circ\text{C})} \quad (3)$$

As shown in Fig. 6e and supplementary Table 5, the Ru SA-rGO/SAM diffusion barrier developed in this work exhibits significantly higher

TTF_{50%} ratio compared to other reported diffusion barriers, while maintaining an ultra-thin thickness. This indicates that the Ru SA-rGO/SAM diffusion barrier is a candidate material for advanced Cu interconnect.

Conductivity

To investigate the influence of different diffusion barriers on interconnect conductivity, Cu/diffusion barrier/SiO₂/Si square samples measuring 20 × 20 mm were prepared. The sheet resistance (R_s) of samples was measured using four-probe method. As shown in Fig. 6f, samples with rGO/SAM and Ru SA-rGO diffusion barrier take a decrease in R_s of 23.4 and 26% compared to Cu/SiO₂/Si samples, respectively. The intercalation of rGO/SAM between Cu film and the SiO₂ substrate effectively improves interconnect conductivity, which might be attributed to the reduction of surface scattering and the provision of an additional conductive path^{58,59}. Based on this, the support of Ru atoms not only repairs the carbon skeleton of rGO, but also provides free electrons to rGO. This achieves a further enhancement of interconnect conductivity.

To explore the underlying mechanism responsible for the significant increase in Cu interconnect conductivity upon introduction of the Ru SA-rGO/SAM diffusion barrier, we deposited Cu films of varying thicknesses (6.5 nm to 182 nm) on both SiO₂ substrate and Ru SA-rGO/SAM/ SiO₂ structure. As verified by AFM in supplementary Figs. 17 and 19, all Cu film thicknesses were precisely measured. For each sample, the resistivity of Cu film was calculated by multiplying the sheet resistance obtained from four-probe method by the corresponding film thickness. The resistivity distribution across different thicknesses for both structures is plotted in Fig. 6g.

Based on the Fuchs-Sondheimer (F-S) model for surface electron scattering resistance and the Mayadas-Shatzkes (M-S) model for grain boundary scattering resistance, the resistivity of thin films can be expressed by the following equation⁹

$$\rho = \rho_0 + \rho_0 \lambda \frac{3(1-p)}{4d} + \rho_0 \lambda \frac{3R}{2D(1-R)} \quad (4)$$

where ρ_0 represents the bulk resistivity, λ is the electron mean free path of the metal, d is the thickness of the metal film, and D is the average grain size. The surface scattering parameter p quantifies electron-surface interactions ($p=0$ for completely diffuse scattering and $p=1$ for completely specular scattering), and the grain boundary scattering parameter R characterizes electron-grain boundary interactions ($R=0$ for completely transmitting and $R=1$ for completely reflecting). Considering all Cu films were deposited under identical conditions (differing solely in deposition time), we may reasonably assume a constant grain boundary reflection parameter R_0 for all samples. Based on this premise and drawing on the material properties of Cu film from reported research⁶⁰ ($\rho_{Cu} = 1.68 \times 10^{-8} \Omega m^{-1}$, $\lambda = 40.0$ nm, $D = k_0 d$, k_0 is a constant), the equation thereby simplifies to:

$$\rho = \rho_0 + \frac{1}{d} \times \rho_0 \lambda \left[\frac{3}{4}(1-p) + \frac{3R_0}{2k_0(1-R_0)} \right] \quad (5)$$

Based on the simplified equation, we performed linear fitting of the $\rho - 1/d$ relationship as shown in Fig. 6h, with the slope and intercept of the fitted curve displayed in supplementary Table 9. While we cannot directly obtain precise ρ values from the $\rho - 1/d$ relationship fitting curves, we can accurately calculate the difference in ρ values ($\Delta\rho$) between the two structures by subtracting the slopes of the two curves:

$$K_1 - K_2 = \frac{3}{4} \rho_0 \lambda (p_2 - p_1) \quad (6)$$

$$\Delta\rho = p_2 - p_1 = \frac{4(K_1 - K_2)}{3\rho_0 \lambda} \quad (7)$$

By substituting the slopes of both curves into the equation, we obtain $\Delta\rho = 0.4986$. This result demonstrates that the introduction of Ru SA-rGO/SAM significantly enhances the transition trend from diffuse to specular electron scattering at the surface, which means the change in surface scattering constitutes a significant contributor to the enhanced conductivity of Cu interconnect.

Mechanism of Cu diffusion blocking of Ru SA-rGO/SAM

Based on the analysis above, the physical and chemical blocking mechanism of Ru SA-rGO/SAM is illustrated in Fig. 7a. On the one hand, the rGO lattice itself can serve as a physical barrier to block Cu vertical diffusion. In addition, the O-containing functional groups in rGO can also have a certain blocking effect on Cu lateral diffusion. After the Ru-supporting process, the small-sized vacancies are occupied by Ru atoms, thus, preventing Cu diffusion physically. Nevertheless, a reasonable explanation is still lacking for the large-sized vacancies in rGO that are more prone to failure.

On the other hand, Ru SA-rGO/SAM can chemically block Cu diffusion by chemical absorption. To further explore the chemical blocking mechanism of Ru SA-rGO/SAM, a 10-atom model was determined as a typical structure. To simulate the process of Cu diffusion through the vacancy model, we set the state with Cu positioned above the vacancy model as the initial state (IS), and the state with Cu positioned below the vacancy model as the final state (FS). Between IS and FS, 9 intermediate states were set based on the distance between Cu and the plane of the vacancy model, where the state with Cu and the vacancy model being on the same plane is considered the transition state (TS). The optimized structures for the rGO, N-rGO and Ru SA-rGO models in different states are shown in Fig. 7b. It can be observed that Cu is absorbed by forming chemical bonding. The potential barrier (E_b) can be defined as $E_b = \Delta E_{ac} - \Delta E_{ai}$, where ΔE_{ac} and ΔE_{ai} represent the adsorption energy of a certain state and IS, respectively. The trend of E_b changing with the states is shown in Fig. 7c. It can be seen that all three models exhibit lower adsorption energy as Cu approaching, and reach a minimum value at TS. Therefore, a more negative value of E_b indicates a stronger chemical blocking ability of diffusion barrier. The E_b value of rGO, N-rGO and Ru SA-rGO vacancy models is -4.06 eV, -5.35 eV and -6.28 eV, respectively. This result elucidates that the N-doping process can enhance the absorption ability to capture Cu, and the subsequent Ru-supporting process can further improve its diffusion barrier properties.

Discussion

In conclusion, a ~1.4 nm Ru SA-rGO/SAM diffusion barrier is fabricated using a BEOL compatible process. The supporting of Ru requires a N-doping process as a bridge. It is demonstrated that Ru species are supported as individual single atoms. Ru SA-rGO/SAM exhibits excellent adhesion to Cu, and possesses outstanding thermal and electrical diffusion barrier properties. The good adhesion of Ru SA-rGO/SAM layer is confirmed by tape adhesion test and morphological characterization. STEM-EDS mapping and XRD patterns prove that Ru

SA-rGO/SAM remains effective under annealing treatment condition of 600 °C for 30 min. Through electrical tests including the I-V and TDB measurement, Ru SA-rGO/SAM shows a 1.33 × critical electric field and a 24 × TTF_{50%} compared to devices without diffusion barrier. Simultaneously, the addition of the Ru SA-rGO/SAM layer can bring about a 26% decrease in R_{\square} . We further elucidated the diffusion blocking mechanism enhanced by Ru SA through DFT calculation. Ru atoms not only physically block Cu diffusion by filling the vacancies in GO, but also chemically capture Cu atoms by enhanced adsorption. Our work provides an approach for the next-generation diffusion barrier, which benefits for the development of advanced interconnect technology.

Methods

Preparation of SAM/SiO₂/Si

The 20 × 20 mm Si substrates with 40 nm thick thermally oxidized SiO₂ were firstly ultrasonically cleaned in acetone, ethanol, and deionized water for 5 min each, in sequence. Piranha solution was prepared by mixing H₂SO₄ and 30% H₂O₂ in a volumetric ratio of 7: 3 with stirring. The cleaned SiO₂/Si substrates were then immersed in the piranha solution at 90 °C for 30 min to achieve surface hydroxylation. The APTES derived SAM was fabricated by immersion of the surface-hydroxylated SiO₂/Si substrate into a 5 mM solution of APTES (in a solvent mixture of acetone and water at a 5: 1 ratio) at room temperature for 30 min. Finally, the SAM/SiO₂/Si samples were rinsed with ethanol and deionized water and dried in an air flow.

Preparation of rGO/SAM/SiO₂/Si

GO was prepared using Hummers method. 0.5 g nano-graphite powder, 0.5 g NaNO₃, and 40 ml H₂SO₄ were firstly added into a flask. The mixture was stirred in an ice bath, and 3 g KMnO₄ was slowly added. The system temperature was then raised to 40 °C and reacted for 90 min. Subsequently, 30 ml water was added, and the reaction was continued maintaining constant temperature for another 30 min. Next, 100 ml water was added to prepare crude GO, followed by the addition of 3 ml 30% H₂O₂ to react with residual oxides. Afterwards, crude GO was centrifuged at 447 g for 2 min to remove the unreacted graphite powder, and then washed four times with deionized water by centrifugation at 7155 g for 15 min per wash cycle. Finally, the washed GO was dissolved in 20 ml water to obtain the GO concentrated solution. 5 ml GO concentrated solution was dispersed in 200 ml water by ultrasonic treatment for 90 min to form GO colloid. Few-layer GO was fabricated on SAM/SiO₂/Si samples using electrophoretic deposition. The SAM/SiO₂/Si samples served as anode and a cleaned Cu foil served as cathode in the GO colloid. A voltage of 30 V was applied for 5 min to drive GO micelles to migrate towards the anode surface. The GO micelles adsorbed on the anode surface and underwent a self-limiting reaction with SAM, achieving the deposition of few-layer GO on SAM/SiO₂/Si samples. The GO/SAM/SiO₂/Si samples were thermally reduced at 200 °C for 2 h in an Ar atmosphere to prepare rGO/SAM/SiO₂/Si samples.

Preparation of N-rGO/SAM/SiO₂/Si and Ru SA-rGO/SAM/SiO₂/Si

During ultrasonic treatment of the GO concentrated solution, N-GO colloid was formed with an extra addition of 250 μl aniline. The remaining steps for the preparation of N-rGO/SAM/SiO₂/Si samples are consistent with those for rGO/SAM/SiO₂/Si samples. Through the final thermal treatment, N species from the stacked aniline were incorporated into the carbon skeleton of GO. To synthesize Ru SA-rGO, after the deposition of few-layer N-GO on SAM, the SAM/SiO₂/Si samples were immersed into a solution containing 1 mM RuCl₃ in water at pH = 1 (adjusted by HCl) for 4 h at room temperature. In the process, Ru species were coordinated with the -NH₂ of aniline in N-GO. The samples were then rinsed by ethanol and deionized water to remove unsupported Ru. The subsequent steps for the preparation

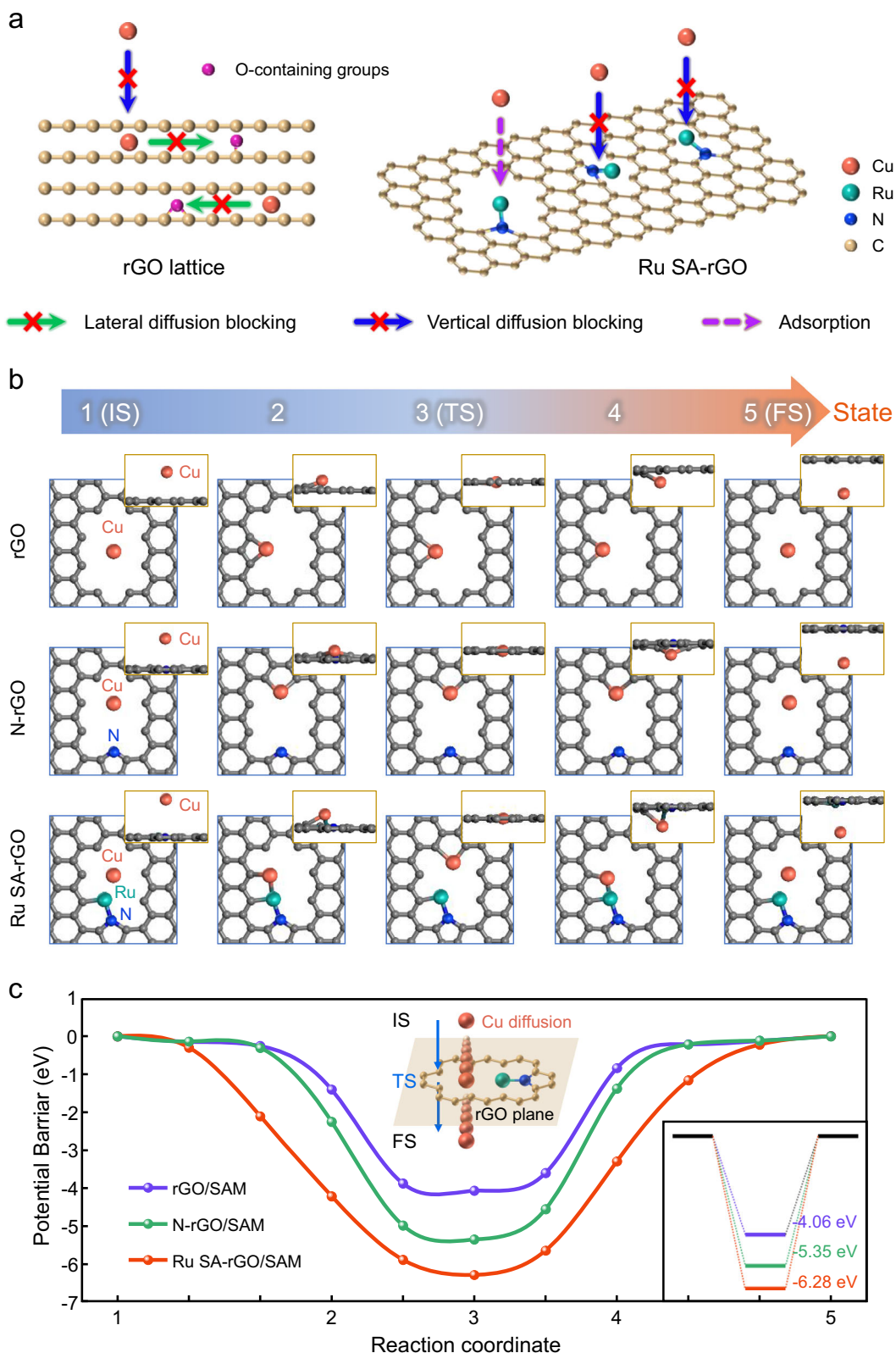


Fig. 7 | Exploration of the mechanism of single atom Ru-supported (Ru SA)-rGO in blocking Cu diffusion. a A Comprehensive mechanism of Ru SA-rGO in blocking Cu diffusion. b The optimized structures (the blue chart represents the top view, and the yellow chart represents the side view) and c the calculated potential barrier

profile of rGO, N-rGO, and Ru SA-rGO vacancy models in different states (The schematic diagram near the curves illustrates the process of the state changes during Cu diffusion). Source data are provided as a Source Data file.

of Ru SA-rGO/SAM/SiO₂/Si samples are consistent with those for rGO/SAM/SiO₂/Si samples. The N-doping process facilitated the anchoring of Ru atoms into GO.

Instrument of characterization and tests

The morphology of samples was characterized using SEM (MIRA3, TESCAN) analysis and TEM (Talos F200X G2, Thermo Scientific) analysis. HAADF-STEM was conducted on a system equipped with spherical aberration corrector and operated at 80 kV. Raman spectra were acquired through confocal microscopic Raman spectrometer (Renishaw inVia Qontor). XPS spectra were carried out to analyze the chemical composition of samples by Thermo Fisher Scientific ESCALAB-250Xi with an Al K α radiation source. Prior to XPS analysis, the samples were ultrasonically cleaned sequentially in ethanol and deionized water to remove surface contaminants. After cleaning and drying, the samples were rapidly transferred to the XPS chamber to minimize air exposure. The details of and parameters used for XPS spectra fitting are shown in supplementary Table 13. The thickness and roughness of samples were measured by AFM (FastScan, Bruker). For thickness measurement, an adhesive tape was applied to protect a designated area on the SiO₂ substrate. Following the sequential deposition of SAM, rGO, and supporting of Ru, the tape was removed prior to annealing to create the thickness step. XRD patterns were collected to determine the phase structures of the samples by Mini Flex 600 with a Cu K α radiation source in a condition of 40 kV, 15 mA at a scan rate of 5° min⁻¹. The sheet resistance was measured by four-point probe station (ST2258C, Suzhou Jingge). I-V measurement and TDDB measurement was tested through Kethley 4200 to evaluate the electrical properties of devices.

DFT structural optimization and calculations

All the computations were performed by the density functional theory (DFT) method with projector augmented wave (PAW) pseudo-potentials using the Perdew-Burke-Ernzerhof (PBE) functional within the generalized gradient approximation (GGA) in the Vienna Ab initio Simulation (VASP 5.4.4)⁶¹⁻⁶³. The plane wave cutoff energy was set as 450 eV. The energy and force convergence threshold were adopted 10⁻⁵ eV and 0.05 eV Å⁻¹ for structural optimizations. The Brillouin zone was sampled by 2 × 2 × 1 *k*-points using the Monkhorst-Pack scheme. The van der Waals interaction between atoms was treated using the DFT-D3 method with Becke-Jonson damping⁶⁴. A vacuum of 27 Å along the z-direction was fixed to avoid interaction between adjacent layers. Solvation effects were taken into account with the VASPsol model using the dielectric constant of water at 78.5⁶⁵. The climbing image nudged elastic band (CI-NEB) method is used to calculate the migration energy of Cu atom diffusing in rGO, N-rGO, and Ru SA-rGO vacancy models⁶⁶.

Statistics and Reproducibility

Data in Figs. 2b–e, h–j, 4d–e, 5b–f are representative of three independent experiments with similar results. Data in Fig. 4b, c are representative of four independent experiments with similar results. Data in Fig. 2k are representative of five independent experiments with similar results.

Reporting summary

Further information on research design is available in the Nature Portfolio Reporting Summary linked to this article.

Data availability

The data that support the findings of this study are available in the supplementary material of this article. Additional information is available from the authors on request. Source data are provided with this paper.

References

1. Salahuddin, S., Ni, K. & Datta, S. The era of hyper-scaling in electronics. *Nat. electron.* **1**, 442–450 (2018).
2. Kim, J. S. et al. Addressing interconnect challenges for enhanced computing performance. *Science* **386**, 6189 (2024).
3. Lau, J. H. “3D IC integration and 3D IC packaging” in *Semiconductor Advanced Packaging* (Springer, 2021).
4. Knoops, H. C. M. et al. Deposition of TiN and TaN by remote plasma ALD for Cu and Li diffusion barrier applications. *J. Electrochem. Soc.* **155**, G287 (2008).
5. Wang, W. L. et al. The reliability improvement of Cu interconnection by the control of crystallized α -Ta/TaN_x diffusion barrier. *J. Nanomater.* **1**, 917935 (2015).
6. Graham, R. L. et al. Resistivity dominated by surface scattering in sub-50 nm Cu wires. *Appl. Phys. Lett.* **96**, 042116 (2010).
7. Gall, D. Metals for low-resistivity interconnects. *2018 IEEE International Interconnect Technology Conference (IITC)* 157–159 (IEEE, 2018).
8. Witt, C. et al. Testing the limits of TaN barrier scaling. *2018 IEEE International Interconnect Technology Conference (IITC)* 54–56 (IEEE, 2018).
9. Moon, J. H. et al. Materials quest for advanced interconnect metallization in integrated circuits. *Adv. Sci.* **10**, 2207321 (2023).
10. Lo, C. L. et al. Opportunities and challenges of 2D materials in back-end-of-line interconnect scaling. *J. Appl. Phys.* **128**, 080903 (2020).
11. Zhang, D. et al. Investigation of barrier property of amorphous Co-Ti layer as single barrier/liner in local Co interconnects. *IEEE Trans. Electron Devices* **67**, 2076–2081 (2020).
12. Mori, Y. et al. Self-formation of a Ru/ZnO multifunctional bilayer for the next-generation interconnect technology via area-selective atomic layer deposition. *Small* **19**, 2300290 (2023).
13. Zhao, Z. et al. Aminosilanization nanoadhesive layer for nanoelectric circuits with porous ultralow dielectric film. *ACS Appl. Mater. Interfaces* **5**, 6097–6107 (2013).
14. Fang, J. S. et al. Strengthening the electromigration resistance of nanoscaled copper lines by (3-aminopropyl) trimethoxysilane self-assembled monolayer. *ECS J. Solid State Sci. Technol.* **10**, 083007 (2021).
15. Nguyen, B. S., Lin, J. F. & Perng, D. C. 1-nm-thick graphene tri-layer as the ultimate copper diffusion barrier. *Appl. Phys. Lett.* **104**, 082105 (2014).
16. Lo, C. L. et al. Atomically thin diffusion barriers for ultra-scaled Cu interconnects implemented by 2D materials. *2017 IEEE International Reliability Physics Symposium (IRPS)* MR-4.1-MR-4.4 (IEEE, 2017).
17. Smithe, K. K. et al. Investigation of monolayer MX 2 as sub-nanometer copper diffusion barriers. *2018 IEEE International Reliability Physics Symposium (IRPS)* P-PI.1-1-P-PI.1-4 (IEEE, 2018).
18. Lo, C. L. et al. Enhancing interconnect reliability and performance by converting tantalum to 2D layered tantalum sulfide at low temperature. *Adv. Mater.* **31**, 1902397 (2019).
19. Deijkers, J. S. H. et al. MoS₂ synthesized by atomic layer deposition as Cu diffusion barrier. *Adv. Mater. Interfaces* **10**, 2202426 (2023).
20. Caro, A. M. et al. Screening self-assembled monolayers as Cu diffusion barriers. *Microelectron. Eng.* **85**, 2047–2050 (2008).
21. Zhang, Y. P., Sil, M. C. & Chen, C. M. Organosiloxane nanolayer as diffusion barrier for Cu metallization on Si. *Appl. Surf. Sci.* **567**, 150800 (2021).
22. Caro, A. M. et al. Bottom-up engineering of subnanometer copper diffusion barriers using NH₂-derived self-assembled monolayers. *Adv. Funct. Mater.* **20**, 1125–1131 (2010).
23. Liu, H. et al. Thermal stability of self-assembled 3-aminopropyl-trimethoxysilane diffusion barrier terminated by carboxyl groups. *Appl. Sci.* **12**, 11098 (2022).

24. Chung, Y. et al. Coupled self-assembled monolayer for enhancement of Cu diffusion barrier and adhesion properties. *RSC Adv.* **4**, 60123–60130 (2014).

25. Hsu, B. F. et al. Functionalizing self-assembled monolayers to reduce interface scattering in ruthenium/dielectric for next-generation microelectronic interconnects. *Appl. Surf. Sci.* **645**, 158870 (2024).

26. Chou, Y. W., Chang, S. Y. & Keng, P. Y. Thermal stability and orthogonal functionalization of organophosphonate self-assembled monolayers as potential liners for Cu interconnect. *ACS Omega* **8**, 39699–39708 (2023).

27. Sil, C. M. et al. Effects of molecular assembly on heterogeneous interactions in electronic and photovoltaic devices. *Chem. Phys. Rev.* **5**, 011301 (2024).

28. Li, L. et al. Vertical and lateral copper transport through graphene layers. *ACS nano* **9**, 8361–8367 (2015).

29. Roy, S. S. & Arnold, M. S. Improving graphene diffusion barriers via stacking multiple layers and grain size engineering. *Adv. Funct. Mater.* **23**, 3638–3644 (2013).

30. Lo, C. L. et al. Studies of two-dimensional h-BN and MoS₂ for potential diffusion barrier application in copper interconnect technology. *npj 2D Mater. Appl.* **1**, 42 (2017).

31. Wang, J. et al. The rare two-dimensional materials with Dirac cones. *Natl. Sci. Rev.* **2**, 22–39 (2015).

32. Lee, H. C. et al. Toward near-bulk resistivity of Cu for next-generation nano-interconnects: graphene-coated Cu. *Carbon* **149**, 656–663 (2019).

33. Son, M. et al. Copper-graphene heterostructure for back-end-of-line compatible high-performance interconnects. *npj 2D Mater. Appl.* **5**, 41 (2021).

34. Shin, K. W. et al. Graphene capping of Cu back-end-of-line interconnects reduces resistance and improves electromigration lifetime. *ACS Appl. Nano Mater.* **6**, 4170–4177 (2023).

35. Neto, A. H. C. et al. The electronic properties of graphene. *Rev. mod. Phys.* **81**, 109–162 (2009).

36. Zhao, Y. et al. Mass transport mechanism of Cu species at the metal/dielectric interfaces with a graphene barrier. *ACS nano* **8**, 12601–12611 (2014).

37. Lee, J. H. et al. Wafer-scale growth of single-crystal monolayer graphene on reusable hydrogen-terminated germanium. *Science* **344**, 286–289 (2014).

38. Gao, L. et al. Face-to-face transfer of wafer-scale graphene films. *Nature* **505**, 190–194 (2014).

39. Yuan, G. et al. Proton-assisted growth of ultra-flat graphene films. *Nature* **577**, 204–208 (2020).

40. Hoofman, R. et al. Challenges in the implementation of low-k dielectrics in the back-end of line. *Microelectron. Eng.* **80**, 337–344 (2005).

41. Novoselov, K. S. et al. A roadmap for graphene. *Nature* **490**, 192–200 (2012).

42. Mehta, R., Chugh, S. & Chen, Z. Transfer-free multi-layer graphene as a diffusion barrier. *Nanoscale* **9**, 1827–1833 (2017).

43. Yuan, G. et al. Stacking transfer of wafer-scale graphene-based van der Waals superlattices. *Nat. Commun.* **14**, 5457 (2023).

44. Bong, J. H. et al. Ultrathin graphene and graphene oxide layers as a diffusion barrier for advanced Cu metallization. *Appl. Phys. Lett.* **106**, 063112 (2015).

45. Urade, A. R., Lahiri, I. & Suresh, K. S. Graphene properties, synthesis and applications: a review. *Jom* **75**, 614–630 (2023).

46. Yu, L. et al. A graphene oxide oxygen barrier film deposited via a self-assembly coating method. *Synth. Met* **162**, 710–714 (2012).

47. Sharma, S. et al. Deposition and characterization of 3-aminopropyltrimethoxysilane monolayer diffusion barrier for copper metallization. *Metall. Mater. Trans. B* **46**, 928–932 (2015).

48. Besra, L. & Liu, M. A review on fundamentals and applications of electrophoretic deposition (EPD). *Prog. Mater. Sci.* **52**, 1–61 (2007).

49. Ye, S. et al. Highly stable single Pt atomic sites anchored on aniline-stacked graphene for hydrogen evolution reaction. *Energy Environ. Sci.* **12**, 1000–1007 (2019).

50. López-Díaz, D. et al. Evolution of the Raman spectrum with the chemical composition of graphene oxide. *J. Phys. Chem. C* **12**, 20489–20497 (2017).

51. Avcu, E. et al. The effect of reduced graphene oxide content on the microstructural and mechanical properties of copper metal matrix composites. *Mater. Sci. Eng. A* **856**, 143921 (2022).

52. Zhang, Y. et al. N-doped graphene supported Cu single atoms: Highly efficient recyclable catalyst for enhanced C–N coupling reactions. *ACS nano* **16**, 1142–1149 (2022).

53. Morgan, D. J. Resolving ruthenium: XPS studies of common ruthenium materials. *Surf. Interface Anal.* **47**, 1072–1079 (2015).

54. Chang, S. Y. et al. Mechanical property analyses of porous low-dielectric-constant films for stability evaluation of multilevel-interconnect structures. *Thin Solid Films* **460**, 167–174 (2004).

55. Kim, K. et al. Ultralow-k amorphous boron nitride film for copper interconnect capping layer. *IEEE Trans. Electron Devices* **70**, 2588–2593 (2023).

56. Imtiaz, S. et al. Directly deposited antimony on a copper silicide nanowire array as a high-performance potassium-ion battery anode with a long cycle life. *Adv. Funct. Mater.* **33**, 2209566 (2023).

57. Suzumura, N. et al. A new TDDB degradation model based on Cu ion drift in Cu interconnect dielectrics. *IEEE Int. Reliab. Phys. Symp. Proc.* **2018**, 484–489 (2006).

58. Gall, D. The search for the most conductive metal for narrow interconnect lines. *J. Appl. Phys.* **127**, 050901 (2020).

59. Kuo, C. Y. et al. Graphene-all-around cobalt interconnect with a back-end-of-line compatible process. *Nano Lett.* **24**, 2102–2109 (2024).

60. Chen, L. et al. Interdiffusion reliability and resistivity scaling of intermetallic compounds as advanced interconnect materials. *J. Appl. Phys.* **129**, 035301 (2021).

61. Hafner, J. Ab-initio simulations of materials using VASP: Density-functional theory and beyond. *J. Comput. Chem.* **29**, 2044–2078 (2008).

62. Perdew, J. P., Burke, K. & Ernzerhof, M. Generalized gradient approximation made simple. *Phys. Rev. Lett.* **77**, 3865 (1996).

63. Blöchl, P. E. Projector augmented-wave method. *Phys. Rev. B* **50**, 17953 (1994).

64. Grimme, S. et al. A consistent and accurate ab initio parametrization of density functional dispersion correction (DFT-D) for the 94 elements H–Pu. *J. Chem. Phys.* **132**, 154104 (2010).

65. Mathew, K. et al. Implicit solvation model for density-functional study of nanocrystal surfaces and reaction pathways. *J. Chem. Phys.* **140**, 084106 (2014).

66. Henkelman, G., Uberuaga, B. P. & Jónsson, H. A climbing image nudged elastic band method for finding saddle points and minimum energy paths. *J. Chem. Phys.* **113**, 9901–9904 (2000).

Acknowledgements

This work was supported by the National Natural Science Foundation of China (No. 22472095, Y.W.). This work was supported by the Shanghai Municipal Education Commission Research Project (No. 2024A1ZD012, S.J.) and Shanghai International Science and Technology Collaboration Project (No. 24160712600, S.J.). This work was supported by Fundamental Research Funds for the Central Universities (No. YG2025ZD13, Y.W.).

Author contributions

Conceptualization: Y.W. Data curation: G.C. Investigation: S.Z. and D.Z. Methodology: S.Z., D.Z., and X.R. Resources: Y.W., G.C., S.J., T.H., and

M.L. Software: S.J. Supervision: Y.W. and S.J. Visualization: S.Z., D.Z., and Y.W. Writing – original draft: S.Z. and D.Z. Writing – review & editing: Y.W., S.J., and T.H.

Competing interests

The authors declare no competing interests.

Additional information

Supplementary information The online version contains supplementary material available at <https://doi.org/10.1038/s41467-025-67668-7>.

Correspondence and requests for materials should be addressed to Shenghong Ju or Yunwen Wu.

Peer review information *Nature Communications* thanks the anonymous, reviewers for their contribution to the peer review of this work. A peer review file is available.

Reprints and permissions information is available at <http://www.nature.com/reprints>

Publisher's note Springer Nature remains neutral with regard to jurisdictional claims in published maps and institutional affiliations.

Open Access This article is licensed under a Creative Commons Attribution-NonCommercial-NoDerivatives 4.0 International License, which permits any non-commercial use, sharing, distribution and reproduction in any medium or format, as long as you give appropriate credit to the original author(s) and the source, provide a link to the Creative Commons licence, and indicate if you modified the licensed material. You do not have permission under this licence to share adapted material derived from this article or parts of it. The images or other third party material in this article are included in the article's Creative Commons licence, unless indicated otherwise in a credit line to the material. If material is not included in the article's Creative Commons licence and your intended use is not permitted by statutory regulation or exceeds the permitted use, you will need to obtain permission directly from the copyright holder. To view a copy of this licence, visit <http://creativecommons.org/licenses/by-nc-nd/4.0/>.

© The Author(s) 2025